RSC Advances

PAPER

View Article Online
View Journal | View Issue

Cite this: *RSC Adv.*, 2026, **16**, 25732

New organic–inorganic bromide $(P(C_4H_9)_4)_2[ZnBr_4]$: crystal structure, vibrational properties, and electrical conduction behavior from impedance studies

Molka Ezzedine, *[a] Malika Ben Gzaiel, [ab] Mohamed Tliha,[c] E. López-Lago,[d] Walid Rekik,[e] Ali Ben Ahmed [f] and Abderrazek Oueslati [a]

There has been a lot of interest in the development of a novel hybrid material based on zinc with fascinating structural and physical properties. In this paper, a novel organic–inorganic hybrid $(P(C_4H_9)_4)_2[ZnBr_4]$ crystal was synthesized *via* the slow evaporation method at room temperature and characterized by single-crystal X-ray diffraction, supported by density functional theory, vibrational spectroscopy and electrical analysis. At room temperature, it crystallizes in the monoclinic system ($P2_1/c$ space group) with cell parameters a = 15.3260(11) Å, b = 17.6692(13) Å, c = 16.9898(11) Å, β = 114.715(2)°, V = 4179.4(5) Å^3 and Z = 4. Its structure comprises two crystallographically independent organic $(P(C_4H_9)_4)^+$ cations and one type of isolated $[ZnBr_4]^{2-}$ anion. Each tetrahedral $[ZnBr_4]^{2-}$ anion is surrounded by three tetrabutylphosphonium cations, forming multiple C–H···Br contacts that reinforce the structural framework. The density functional theory (DFT)-calculated Raman and IR spectra are in excellent agreement with the experimental data, allowing unambiguous assignment of vibrational modes, including metal–halogen stretches and the dynamics of the organic cations. Electrical impedance spectroscopy demonstrates temperature- and frequency-dependent conductivity with a negative temperature coefficient of resistance, indicating thermistor-like behavior. AC conductivity follows Jonscher's universal power law and is well described by the correlated barrier hopping model. These multifaceted findings establish $(P(C_4H_9)_4)_2[ZnBr_4]$ as a multifunctional hybrid material suitable for integration into next-generation electronic and optoelectronic devices.

Received 31st January 2026
Accepted 27th April 2026

DOI: 10.1039/d6ra00849f

rsc.li/rsc-advances

1 Introduction

The interplay between organic and inorganic components of hybrid materials has garnered significant attention due to the potential emergence of novel physical and chemical properties. This synergy offers new avenues for scientific investigation and technological development.[1] Organic–inorganic hybrid compounds have been widely studied for their diverse functionalities, particularly in areas such as electrical and magnetic behavior, charge transport, luminescence, and optical performance.[2] These materials have found practical applications across multiple sectors, including medicine, pharmaceuticals, and biomedicine;[3] energy storage systems, such as advanced batteries;[4] solar energy harvesting and luminescence-based sensing technologies;[5] and electronics and electrical devices.[6] Consequently, they serve as key contributors to progress across numerous scientific and industrial domains. Among the various subclasses of organic–inorganic materials, those adopting the general formula A_2MX_4, where A represents an organic cation, M represents a transition metal (Co, Cu, Zn, Fe, Cd, Hg, and Mn) and X represents a halide (Cl, Br, and I), have attracted considerable attention.[7,8] These materials exhibit remarkable physicochemical properties and structural diversity, ranging from zero-dimensional molecular clusters and one-dimensional chains to two-dimensional layered architectures and even three-dimensional frameworks. Numerous analogous compounds have been described in the literature, including $[N(C_3H_7)_4]_2HgBr_4$,[9] $[N(C_3H_7)_4]_2ZnBr_4$,[10] $[N(CH_3)_4]_2CoCl_4$,[11] $[N(C_2H_5)_4]_2Cu_2I_4$ (ref. 12) and $[(C_4H_9)_4P]_2Cd_2Cl_6$.[13] These examples illustrate the

[a]*Laboratory of Spectroscopic Characterization and Optical Materials, Faculty of Sciences, University of Sfax, B.P. 1171, 3000 Sfax, Tunisia. E-mail: ezzeddinemolka0@gmail.com*

[b]*University of Gafsa, Higher Institute of Social Sciences and Education, Gafsa, 2119, Tunisia*

[c]*Department of Physics, Al-Qunfudah University College, Umm Al-Qura University, Mecca, Saudi Arabia*

[d]*Departamento de Física Aplicada, Facultade de Óptica e Optometríae Instituto de Materiais (iMATUS) Campus Vida, Universidade de Santiago de Compostela (USC), 15782 Galicia, Spain*

[e]*Laboratory Physical-Chemistry of Solid State, Chemistry Department, Faculty of Sciences of Sfax, University of Sfax, BP 1171, Sfax, 3000, Tunisia*

[f]*Laboratory of Applied Physics, Department of Physics, Faculty of Sciences of Sfax, University of Sfax, Sfax, Tunisia*

structural richness and wide variety of architectures present in alkylphosphonium tetrahalometalates(II). The halogenozincatate(II) class is particularly interesting in this regard. Their structural and functional characteristics are strongly influenced by their ability to form hydrogen bonds with organic cations and by the size and symmetry of these cations. Zinc is particularly important for the development of hybrid architectures. Due to their closed-shell d^{10} configuration and relatively large metal–ligand bond lengths, Zn(II) ions can accommodate diverse coordination geometries, such as tetrahedral,[14] square pyramidal, and octahedral.[15]

Additionally, the non-toxic nature of zinc enhances its suitability for a wide range of practical and academic applications.[16] Moreover, zinc halide-based hybrid materials are typically formed through the interaction between zinc halide inorganic units and organic components. These interactions can involve covalent bonds, ionic forces, or various types of hydrogen bonds.[17] Recent investigations have thoroughly examined the impact of Zn^{2+} ions on the structural stability, along with the electronic and electrical properties, in a variety of compounds, such as $[C_8H_{10}NO]_2ZnBr_4$,[18], $[NH_3(CH_2)_4(NH_3)]ZnBr_4$,[19], $[(C_2H_5)_3NH]_2ZnCl_4$,[17] and $(C_5H_6N_2)_2ZnCl_4$.[20] Within this promising field of research, we report the synthesis and characterization of a new hybrid compound, $(P(C_4H_9)_4)_2[ZnBr_4]$, composed of aliphatic organic molecules as the organic component and zinc(II) bromide as the inorganic counterpart. To elucidate its structural and physicochemical properties, a range of experimental techniques has been employed, including single-crystal X-ray diffraction, vibrational spectroscopy, DFT calculations, and impedance spectroscopy. The results provide valuable insight into the compound's charge transport behavior, luminescent behavior, and charge transport mechanisms. These findings contribute to the rational design of hybrid materials with strong potential for optoelectronic and energy-related applications.

2 Experimental

2.1 Synthesis of the $(P(C_4H_9)_4)_2[ZnBr_4]$ crystal

High-quality white single crystals of $(P(C_4H_9)_4)_2[ZnBr_4]$ were grown at room temperature using the slow evaporation method, which is widely used for preparing organic–inorganic hybrid materials.[21] For this purpose, all reagents were purchased from Sigma-Aldrich and used without further purification. In a typical procedure, stoichiometric amounts of $(P(C_4H_9)_4)Br$ (Fluka, 98% purity, 8.88 mmol) (0.3 g) and anhydrous $ZnBr_2$ (Fluka, 99.99% purity, 4.44 mmol) (0.1 g) were dissolved in 10 mL of distilled water in a 2 : 1 molar ratio. The resulting solution was then allowed to evaporate slowly under ambient conditions. Consequently, well-shaped white single crystals suitable for single-crystal X-ray diffraction analysis were obtained after several days (see Fig. 1). The synthesis reaction can be represented as follows:

$$2\left(P(C_4H_9)_4\right)Br + ZnBr_2 \xrightarrow{H_2O} \left(P(C_4H_9)_4\right)_2[ZnBr_4]. \quad (1)$$

The single crystals were rinsed with absolute ethanol, dried in vacuum desiccators, and remained stable for extended periods.

2.2 Characterization techniques

A single crystal of $(P(C_4H_9)_4)_2[ZnBr_4]$ was carefully chosen under a polarizing microscope and mounted at 296(2) K using a Bruker D8 VENTURE PHOTON III-14 diffractometer with Mo Kα radiation ($\lambda = 0.71073$ Å). Absorption corrections were performed using the multi-scan method with the SADABS

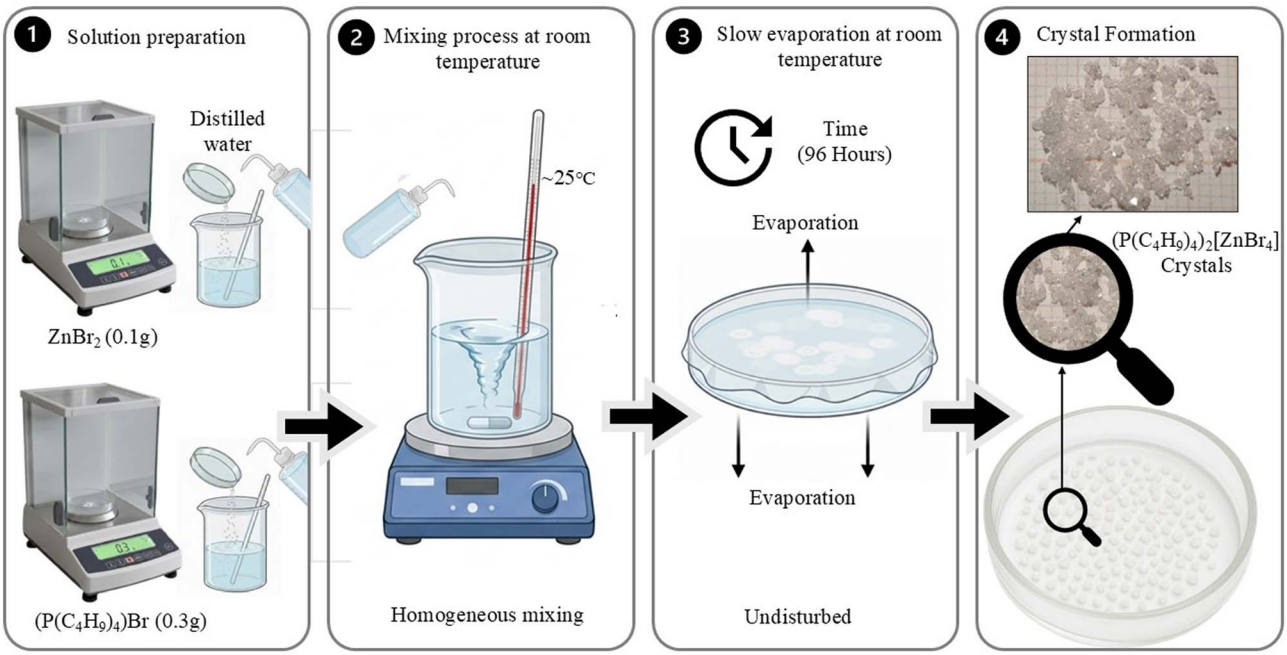

Fig. 1 Synthetic route for the $(P(C_4H_9)_4)_2[ZnBr_4]$ crystals.

Table 1 Crystallographic data and structure refinements of $(P(C_4H_9)_4)_2[ZnBr_4]$

Formula	$(P(C_4H_9)_4)_2[ZnBr_4]$
Color/shape	Colorless/plate
Formula weight (g mol^{-1})	903.84
Crystal system	Monoclinic
Space group	$P2_1/c$
Density	1.436
Crystal size (mm)	0.147 × 0.097 × 0.081
a (Å)	15.3260(11)
b (Å)	17.6692(13)
c (Å)	16.9898(11)
β (°)	114.715(2)
V (Å^3)	4179.4(5)
Z	4

software.[22] The crystal structure, belonging to the monoclinic system with the $P2_1/c$ space group, was initially solved *via* direct methods using the SHELXT-2018 program[23] and subsequently refined using full-matrix least-square methods based on F^2 (SHELXL-2018),[24] assisted by the WINGX program.[25] The anisotropic atomic displacement parameters were refined for all the non-hydrogen atoms. All H atoms were generated geometrically using the HFIX instruction included in SHELXL-2018 (ref. 24) and allowed to ride on their parent atoms with C–H = 0.99 Å and 0.98 Å. The final refinement of F^2 with 8537 unique intensities and 361 parameters converged to excellent reliability factors R_1 = 0.0271 and wR_2 = 0.0678 for 7679 observed reflections with $I > 2\sigma$. Crystal structure drawings were prepared using the Diamond3.2 program.[26] The main crystallographic data are summarized in Tables 1 and S1, while the fractional atomic coordinates and equivalent isotropic temperature factors are detailed in Table S2. The selected bond distances and angles, as well as the hydrogen bonds, are presented in Tables S3 and 2, respectively. Supplementary crystallographic data in CIF format are available from the Cambridge Crystallographic Data Centre (CCDC 2426791) as an electronic supplementary material. These data can be obtained free of charge at https://www.ccdc.cam.ac.uk/data_request/cif.

The phase purity of the $(P(C_4H_9)_4)_2[ZnBr_4]$ compound was examined using a Bruker D8 ADVANCE X-ray diffractometer. X-ray diffraction (XRD) patterns were recorded over an angular range of 5–60° using Cu Kα radiation (λ = 1.5406 Å).

Raman spectra were collected at room temperature in the 50–3200 cm^{-1} range using a Horiba Jobin-Yvon T64000 spectrometer (ISA, Jobin Yvon) on the powdered sample with a 532 nm excitation laser and a 50× microscope objective, which simultaneously focused the beam and collected the backscattered signals. The IR spectrum of the $(P(C_4H_9)_4)_2[ZnBr_4]$ compound was recorded using a PerkinElmer FT-IR 1000 spectrometer over 400–3500 cm^{-1} with a resolution of 0.5 cm^{-1} using a sample of pure KBr dispersed and pressed into a pellet.

All calculations were carried out within the framework of density functional theory (DFT) using the hybrid B3LYP exchange–correlation functional, as implemented in the Gaussian 16 software package, with the LANL2DZ and 6-311G(d,p) basis sets applied to all atoms.

Thermogravimetric analysis (TGA) was performed with an ATG-Q500 SETARAM in a heating process from room temperature up to 850 K at a heating rate of 10 K min^{-1}.

Impedance measurements of the $(P(C_4H_9)_4)_2[ZnBr_4]$ compound were conducted using a two-electrode setup with platinum contacts. Finely ground powder was compressed into cylindrical pellets (8 mm in diameter and 1 mm in thickness) under a pressure of 3 tons cm^{-2}. Ultra-thin gold layers, just a few nanometers thick, were manually applied to both flat surfaces of the pellets. Electrical characterization was carried out using a Solartron 1260 Impedance Analyzer over a frequency ranging from 20 Hz to 1 MHz and a temperature ranging from 303 to 328 K.

Table 2 Electrical fitted circuit parameters for $(P(C_4H_9)_4)_2[ZnBr_4]$ at different temperatures

T (K)	R (×10^6 Ω)	Q (×10^{-11} F)	α
303	5.17	9.45	0.94
308	3.90	8.40	0.943
313	3.15	6.78	0.95
318	2.41	7.40	0.95
323	1.68	8.40	0.95
328	1.03	5.73	0.965

3 Results and discussions

3.1 Structural studies

The hybrid material $(P(C_4H_9)_4)_2[ZnBr_4]$ adopts monoclinic symmetry and crystallizes at 296 K in the $P2_1/c$ space group. As listed in Table 1, the unit cell parameters are as follows: a = 15.3260(11) Å, b = 17.6692(13) Å, c = 16.9898(11) Å, β = 114.715(2)°, V = 4179.4(5) Å^3 and Z = 4. Its 0D structure consists of isolated $[ZnBr_4]^{2-}$ anions and $(P(C_4H_9)_4)^+$ organic cations, interconnected *via* weak C–H···Br interactions, as shown in Fig. 2 and summarized in Table 2.

The asymmetric unit of $(P(C_4H_9)_4)_2[ZnBr_4]$, depicted in Fig. S1, contains only one Zn(II) cation, linked to four Br^- anions, and two crystallographically independent organic cations $(P(C_4H_9)_4)^+$. It should be noted that all atoms occupy general positions (Wyckoff site 4e).

The Zn(II) cation occupies a general position and is coordinated by four bromide ions. The $[ZnBr_4]^{2-}$ complex can adopt one of three geometries: tetrahedral, square planar, or seesaw. To determine the geometry of the zinc polyhedron, we calculated the τ_4 parameter (τ_4 = 0 for a square plane geometry and τ_4 = 1 for a tetrahedral form) using the following formula:

$$\tau_4 = \frac{360 - (\alpha + \beta)}{360 - 2\theta}, \quad (2)$$

where α and β represent the two largest angles in the polyhedron and θ is the angle in a regular tetrahedron (θ = 109.5°). For our calculation, α = 115.254° and β = 110.828°, resulting in τ_4 = 0.949. This indicates that the zinc polyhedron adopts a tetrahedral geometry.

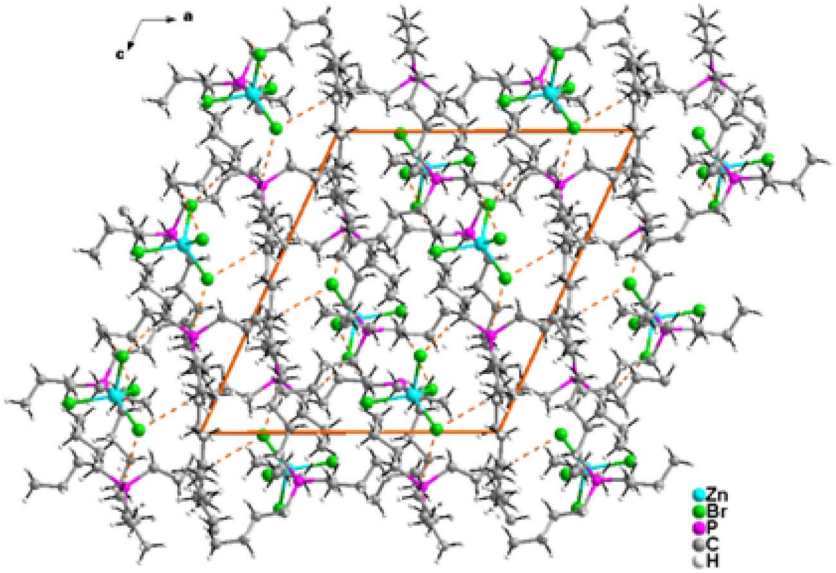

Fig. 2 Projection of the structure of $(P(C_4H_9)_4)_2[ZnBr_4]$ along the crystallographic *b*-axis.

It is important to note that there is no connectivity between the metallic tetrahedra because they are well separated. The shortest Zn–Zn intermetallic distance is 9.0945(7) Å. Within the $[ZnBr_4]^{2-}$ tetrahedra, the Zn–Br bond lengths range from 2.4127(4) to 2.4450(4) Å, while the Br–Zn–Br bond angles vary from 106.402(15)° to 115.254(18)° (Table S3). These values are consistent with those reported for other compounds containing $ZnBr_4$ tetrahedra.[27] Based on the geometric characteristics of the $[ZnBr_4]^{2-}$ anions, the average distortion indices (DI) were calculated using the following equations as follows:[28]

$$\mathrm{DI(Zn-Br)} = \sum_{i=1}^{n_1} \frac{|d_i - d_m|}{n_1 d_m}, \quad (3)$$

$$\mathrm{DI(Br-Zn-Br)} = \sum_{i=1}^{n_2} \frac{|a_i - a_m|}{n_2 a_m}, \quad (4)$$

where "*d*" represents the Zn–Br bond length, "*a*" represents the Br–Zn–Br bond angle, and d_m and a_m are their respective average values. For a tetrahedral environment, $n_1 = 4$ and $n_2 = 6$.

The calculated distortion indices, DI (Zn–Br) = 0.0040 and DI (Br–Zn–Br) = 0.0231, indicate a slight deviation of the $ZnBr_4$ polyhedron from the ideal tetrahedral geometry. This distortion is attributed to the intermolecular C–H···Br interactions between the organic cations and the metallic tetrahedra.

The negative charges of the $[ZnBr_4]^{2-}$ tetrahedra are balanced by tetrabutylphosphonium cations $(P(C_4H_9)_4)^+$. The main distances and angles for these organic cations, shown in Table S3, are in good agreement with those found in other compounds containing the same organic cation.[29,30] Weak C–H···Br interactions connect the inorganic anions with the organic cations. Indeed, each metallic tetrahedron is linked to three tetrabutylphosphonium cations, and each organic cation is involved in C–H···Br interactions with one or two $[ZnBr_4]^{2-}$ anions (Fig. 2 and S2(a, b)). Within these intermolecular C–H···Br interactions, the C···Br distances range from 3.712(3) to 3.828(3) Å, and the C–H···Br angles vary from 138.1° to 165.9° (Table S4).

Rietveld profile refinements carried out using the FullProf software,[31] as shown in Fig. 3, indicate that the compound crystallizes in the monoclinic crystal system with the $P2_1/c$ space group. The refined unit-cell parameters for $(P(C_4H_9)_4)_2[ZnBr_4]$ were determined to be $a = 15.326$ Å, $b = 17.669$ Å, $c = 17.989$ Å, and $\beta = 114.716°$. The quality of the refinement was evaluated through the goodness of fit with $\chi^2 = 4.42$. The values of the reliability factors obtained from the refinement are $R_{wp} = 16.9$, $R_p = 10.4$ and $R_{exp} = 8.06$. The fitted parameters are in close agreement with previously reported single-crystal X-ray diffraction results, confirming the successful synthesis of the target phase along with its structural integrity and high purity.

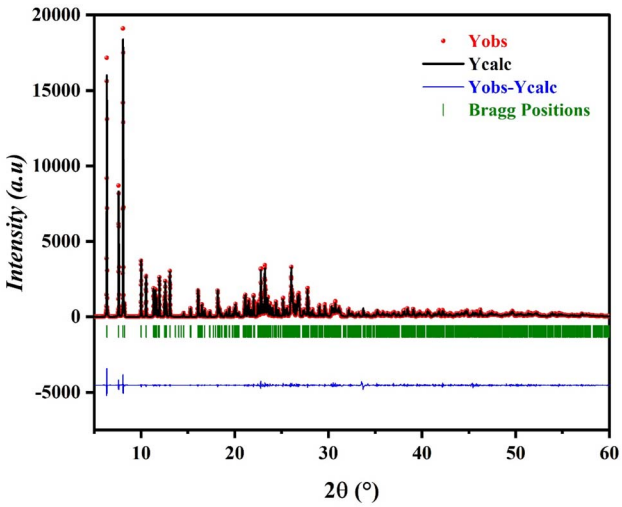

Fig. 3 Profile refinement of the powder X-ray diffraction (PXRD) pattern of the compound $(P(C_4H_9)_4)_2[ZnBr_4]$ using the FullProf software.

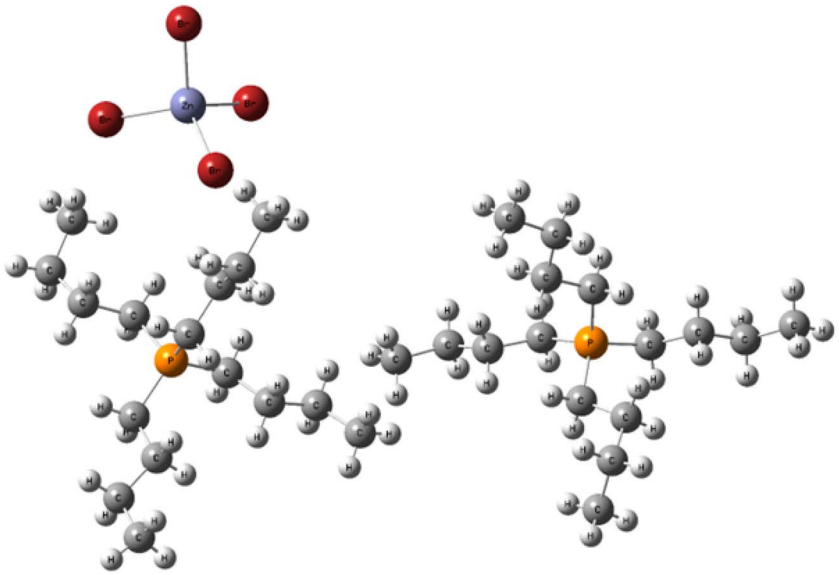

Fig. 4 Optimized geometry of $(P(C_4H_9)_4)_2[ZnBr_4]$.

3.2 Optimized geometry and computational details

Geometry optimizations and vibrational frequency calculations were performed using the B3LYP functional,[32] including Grimme's D3 dispersion correction with Becke–Johnson damping,[33] as implemented in the Gaussian 16 software package.[34] A mixed basis set approach was adopted; Zn and Br atoms were described using the LANL2DZ[35] effective core potential, while C, H, and P atoms were treated with the 6-311G(d,p) basis set.[36] This combination ensures an accurate description of both the metal center and the organic moieties, as well as the weak non-covalent interactions governing the crystal packing. All optimized structures were confirmed as true minima by the absence of imaginary frequencies. The optimized geometry (Fig. 4) exhibits a stable coordination environment, with bond lengths and bond angles lying within the typical ranges reported for structurally related compounds. The reliability of the optimized structure is further supported by the good agreement observed between the experimental and calculated vibrational frequencies, confirming the internal consistency of the computational approach.

3.3 Vibrational spectroscopy and mode assignment

The vibrational properties of the compound were investigated by means of experimental infrared (IR) and Raman spectroscopy and compared with DFT-calculated harmonic frequencies. The calculated spectra reproduce the main experimental features with satisfactory accuracy (Fig. 5 and 6), allowing a reliable assignment of the observed vibrational modes. Minor differences between experimental and theoretical wavenumbers are observed, which can be attributed to anharmonic effects, crystal packing interactions, and temperature effects not explicitly considered in the calculations. Nevertheless, the overall agreement confirms the suitability of the computational model for vibrational interpretation.

The low-wavenumber region is dominated by vibrations involving heavy atoms and collective lattice motions. The experimental bands observed at 155, 212, and 252 cm^{-1} are well reproduced by the calculated modes at 152, 212, and 259 cm^{-1}, respectively. These bands are assigned to lattice vibrations and metal–halogen stretching and bending modes of the inorganic framework. Similar low-frequency features have been commonly reported for metal–halide and hybrid compounds, where the presence of heavy atoms leads to vibrational modes below 300 cm^{-1}.

The spectral region between 300 and 900 cm^{-1} is characterized by skeletal deformations and out-of-plane bending vibrations. The IR band observed at 454 cm^{-1}, which is in excellent agreement with the calculated value, is attributed to the metal–ligand bending modes. The bands appearing in the 700–760 cm^{-1} range are assigned to the C–H out-of-plane bending and framework deformation modes. Additional vibrations observed between 814 and 920 cm^{-1} mainly arise from coupled C–C and C–N stretching vibrations associated with the organic moiety.

The fingerprint region [900–1600 cm^{-1}] exhibits several characteristic bands that provide detailed insight into the bonding environment. The modes observed between 962 and 1110 cm^{-1} are attributed to C–N and C–C stretching vibrations, showing good agreement between the experimental and calculated frequencies. The bands in the 1230–1322 cm^{-1} range originate mainly from C–N stretching coupled with in-plane C–H bending vibrations. The strong features observed between 1370 and 1485 cm^{-1} are assigned to CH_2/CH_3 deformation modes and aromatic ring stretching vibrations. The Raman-active band around 1508–1520 cm^{-1} is characteristic of symmetric ring stretching vibrations. These assignments are consistent with previously reported vibrational studies of structurally related compounds.

The high-wavenumber region [2800–3000 cm^{-1}] is dominated by C–H stretching vibrations of the organic groups. The experimental bands observed between 2862 and 2960 cm^{-1} are

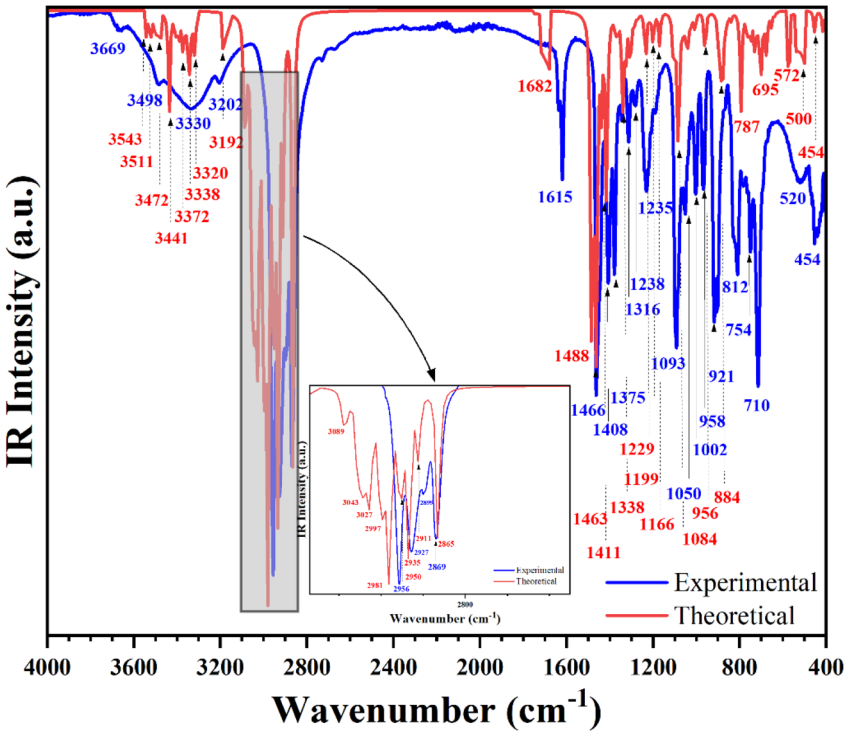

Fig. 5 Experimental and theoretical IR spectra.

satisfactorily reproduced by the calculated frequencies in the 2868–2963 cm^{-1} range. The lower-frequency bands correspond to symmetric CH_2/CH_3 stretching modes, while the higher-frequency bands are attributed to antisymmetric stretching vibrations. This behavior is typical of alkyl-containing ligands and agrees well with the reported data for similar systems.

A comparison with recently published vibrational analyses of analogous compounds reveals a similar distribution of vibrational modes across the low-, mid-, and high-frequency regions. The presence of low-frequency lattice modes, well-defined fingerprint bands, and characteristic C–H stretching vibrations confirms that the present compound shares common structural and bonding features with related systems.

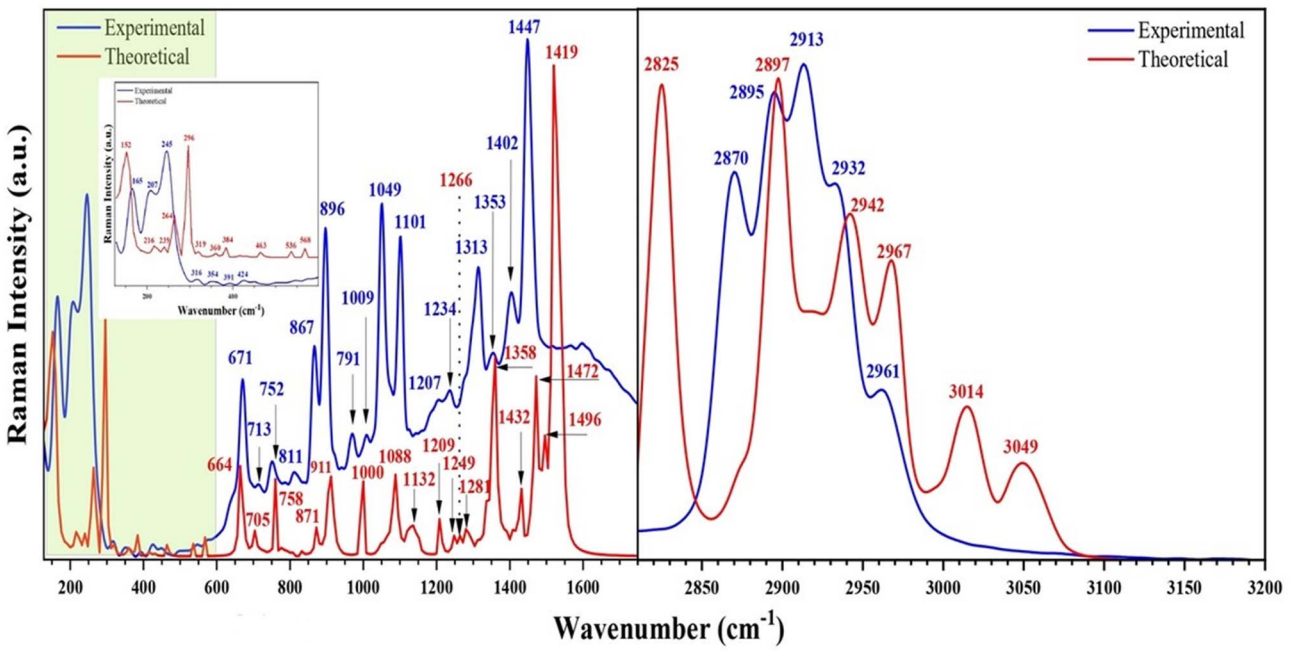

Fig. 6 Experimental and theoretical Raman spectra.

3.4 TGA analysis

Fig. 7 shows the thermogravimetric analysis (TGA) of the $(P(C_4H_9)_4)_2ZnBr_4$ compound. The TGA curve shows that this compound started to decompose at 615 K. Besides, no weight losses were observed between 300 and 615 K.

3.5 Electrical properties

3.5.1 Impedance analysis. Impedance measurements represent a reliable and insightful technique for investigating the electrical properties and ionic transport mechanisms in hybrid materials over a wide range of frequencies.[37] This method is particularly effective in distinguishing between various conduction processes and assessing their individual contributions. In the present study, we focused on examining the electrical response of the $(P(C_4H_9)_4)_2[ZnBr_4]$ material within a temperature range close to room temperature (303–328 K).

Through complex impedance spectroscopy, it is possible to detect the diverse electrical responses present within the system. Accordingly, the following equation can be used:

$$Z^* = Z'(\omega) + jZ''(\omega), \quad (5)$$

where Z' and Z'' represent the real and imaginary components of the complex impedance, respectively.

The Nyquist plot ($-Z''$ *vs.* Z') reveals a single semicircular arc with its center located below the real axis, as illustrated in Fig. 8. This characteristic behavior suggests a deviation from ideal Debye-type relaxation and supports the use of the Cole–Cole model to describe the system's dielectric response.[38] Furthermore, a detailed analysis shows that with increasing temperature, the diameter of the semicircle decreases, indicating a reduction in grain resistance. This trend confirms that the conduction mechanism is thermally activated across the entire temperature range investigated. The semicircular feature observed in the Nyquist plot was modeled using the Z-view software,[39] employing an equivalent circuit consisting of a single element: a parallel configuration of resistance (R) and a constant phase element (CPE), as illustrated in the inset of Fig. 8. In this model, R represents the grain boundaries resistance, and CPE accounts for the non-ideal capacitive behavior, which is often associated with distributed relaxation times. This configuration suggests that the electrical response in the analyzed frequency range is predominantly governed by grain boundary-related processes.[38] The corresponding circuit parameters are summarized in Table 2, which shows that the resistance (R) decreases with increasing temperature. In hybrid materials, grain boundary resistance generally decreases as temperature increases due to the thermal activation of localized charge carriers. This activation increases carrier mobility, thereby facilitating hopping conduction and leading to a reduction in overall resistive behavior as the temperature increases.[40,41]

Fig. 9(a) presents the variation of $Z'(\omega)$ with temperature. It is evident that the real part of the impedance Z' decreases with increasing temperature and frequency, indicating a negative temperature coefficient of resistance (NTCR) behavior in the material.[42] This trend can be attributed to a decrease in trapped charge density and an enhancement in charge carrier mobility within $(P(C_4H_9)_4)_2[ZnBr_4]$ compound, suggesting a possible increase in AC conductivity. At higher frequencies, Z' becomes nearly independent of temperature, implying the presence of a space charge within the material. As frequency increases, the time available for space charge relaxation diminishes. Consequently, at high frequencies, the curves converge due to the suppression of space charge polarization effects.[43]

Fig. 9(b) illustrates the frequency-dependent variation of the imaginary part of impedance ($-Z''$) at temperatures ranging from 303 K to 328 K. The frequency and temperature dependence of Z'' provides valuable insight into the polarization and charge transport mechanisms within the material. At intermediate frequencies, Z'' exhibits well-defined relaxation peaks that move to higher frequencies with increasing temperature, corresponding to characteristic relaxation frequencies (ω_r) linked to charge carrier hopping between localized states. This shift with temperature suggests a thermally activated relaxation

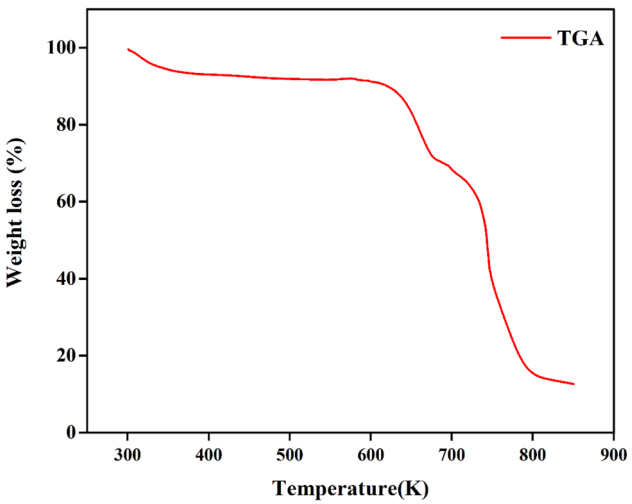

Fig. 7 TGA curve of $(P(C_4H_9)_4)_2[ZnBr_4]$.

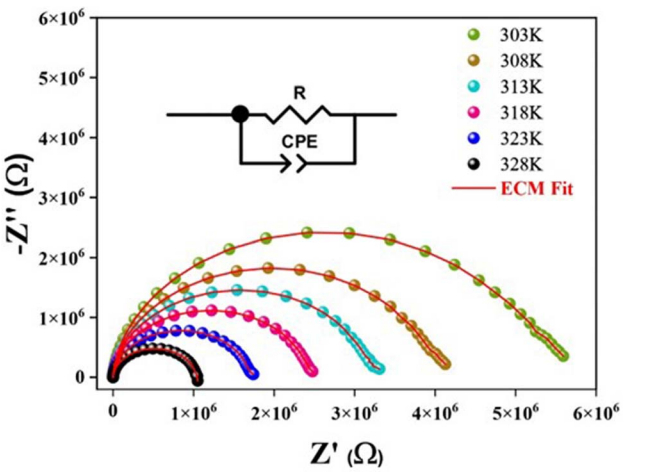

Fig. 8 Nyquist plots and the equivalent circuit model of $(P(C_4H_9)_4)_2[ZnBr_4]$.

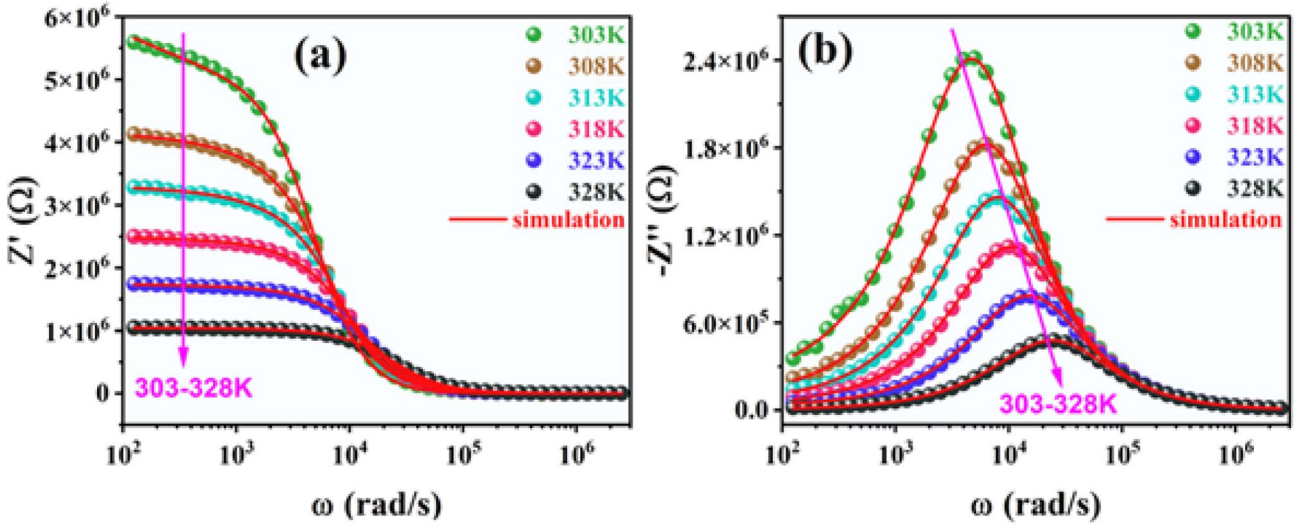

Fig. 9 (a) Variation of the real and (b) imaginary parts of impedance as a function of the frequency.

process in which increased thermal energy enhances the mobility of charge carriers. At lower frequencies, Z'' remains minimal but rises as the frequency approaches ω_r, indicating that static effects, such as interfacial charge buildup, dominate in this region.[40] Beyond ω_r, Z'' decreases with increasing frequency and temperature, reflecting improved conductivity due to enhanced carrier mobility. This trend aligns with the thermally activated conduction mechanism inferred from real impedance (Z') behavior. Moreover, the broadening of Z'' peaks with temperature implies a distribution of relaxation times, likely stemming from the heterogeneous structure of the $(P(C_4H_9)_4)_2[ZnBr_4]$ compound, where both grain and grain boundary contributions are significant. At high frequencies, Z'' approaches zero, suggesting minimal energy loss. This indicates that at such high frequencies, the alternating electric field changes too rapidly for the charge carriers to respond, leading to negligible dielectric losses.

The theoretical values of the real part (Z') and the imaginary part ($-Z''$) of the complex impedance were respectively calculated using the following equations:

$$Z' = \frac{R^{-1} + Q\omega^{\alpha}\cos\left(\frac{\alpha\pi}{2}\right)}{\left(R^{-1} + Q\omega^{\alpha}\cos\left(\frac{\alpha\pi}{2}\right)\right)^2 + \left(Q\omega^{\alpha}\sin\left(\frac{\alpha\pi}{2}\right)\right)^2}, \quad (6)$$

$$-Z'' = \frac{Q\omega^{\alpha} + Q\omega^{\alpha}\sin\left(\frac{\alpha\pi}{2}\right)}{\left(R^{-1} + Q\omega^{\alpha}\cos\left(\frac{\alpha\pi}{2}\right)\right)^2 + \left(Q\omega^{\alpha}\sin\left(\frac{\alpha\pi}{2}\right)\right)^2}. \quad (7)$$

The excellent agreement between the experimental data and the simulated curves, as presented in Fig. 9(a and b), confirms that the proposed equivalent circuit effectively captures the electrical behavior of the studied compound.

To evaluate the activation energies associated with the electrical processes, the resistance values corresponding to the grain boundaries were extracted. Fig. 10 shows the logarithmic variation of resistance as a function of inverse temperature. The resulting plot indicates that this variation follows an Arrhenius-type behavior:[44]

$$R = R_0 \exp\left(\frac{-E_a}{K_B T}\right), \quad (8)$$

where R_0 represents the pre-exponential factor, E_a is the activation energy, K_B is the Boltzmann constant, and T is the absolute temperature. The calculated activation energy is $E_a =$ 0.55 eV for the grain boundary response. This value is comparable to those reported for similar hybrid semiconductor compounds previously described in the literature.[45]

3.5.2 Conductivity mechanism. To gain insight into the electrical conduction mechanism, a thorough investigation of the sample's AC conductivity was carried out. The real component of the electrical conductivity was calculated based on the impedance parameters (Z') and (Z'') using the following expression:[46]

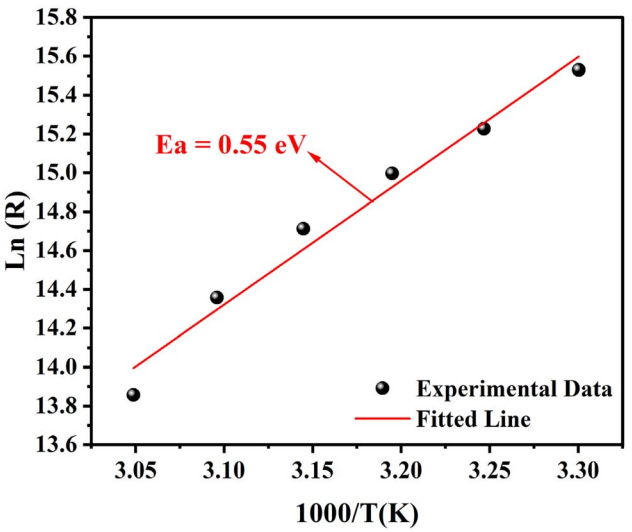

Fig. 10 Variation of ln(R) *versus* 1000/T.

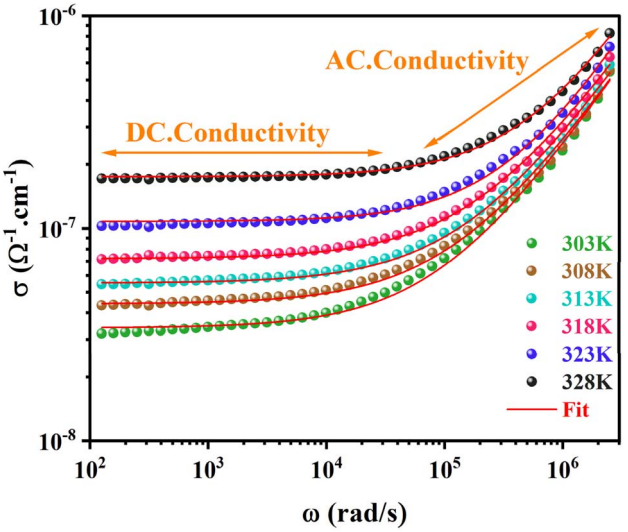

Fig. 11 Frequency dependence of the AC conductivity.

$$\sigma = \frac{e}{s}\frac{Z'}{\left(Z'^2 + Z''^2\right)}, \tag{9}$$

where "*e*" and "*s*" are the thickness and area of the pellet, respectively.

Fig. 11 illustrates how the alternating current conductivity varies with angular frequency at different temperatures (303–328 K) for $(P(C_4H_9)_4)_2[ZnBr_4]$. In the low-frequency region, the curves appear nearly constant, indicating the dominance of a temperature-dependent but frequency-independent DC conductivity component.[47] As the frequency increases, the conductivity values increase markedly, exhibiting pronounced dispersion at higher frequencies, which can be linked to additional dynamic processes.

The frequency at which a noticeable change in conductivity is observed is termed the "hopping frequency" (ω_p), and it shifts to higher values as the temperature increases. This behavior can be explained by the jump relaxation model (JRM) proposed by Funke,[48] which accounts for both the frequency-independent DC conductivity and the frequency-dependent AC response. According to this model, at low frequencies, ions have sufficient time to hop to nearby vacant sites, enabling long-range translational motion that contributes to DC conductivity.

The overall behavior of electrical conductivity is well described by Jonscher's power law, also referred to as the universal dielectric response (UDR) model, among other proposed conduction mechanisms:[49]

$$\sigma(\omega,T) = \sigma_{dc}(T) + \sigma_{ac}(\omega,T), \tag{10}$$

$$\sigma_{ac}(\omega,T) = A(T)\omega^{s(T)}, \tag{11}$$

where A represents a temperature-dependent parameter associated with the material's polarizability, ω denotes the angular frequency, and $s(T)$ is the frequency exponent that characterizes the extent of interaction between the migrating ions and their surrounding matrix. Typically, the exponent $s(T)$ falls within the range of 0 to 1.[50]

As shown in Table S5, the fitted conductivity data indicate that parameter A increases as temperature increases, implying improved charge carrier mobility. Furthermore, the temperature-dependent growth of DC conductivity (σ_{dc}), illustrated in Fig. 12(a), supports the classification of the studied compound as a semiconductor. To evaluate the activation energy at low frequency (20 Hz), the variation of grain conductivity with temperature is analyzed by plotting $\ln(\sigma_{dc} \times T)$ against the inverse temperature, as shown in Fig. 12(b).

The plot displays a linear region following Arrhenius-type behavior, which can be described by the following equation:[37]

$$\sigma_{dc} \times T = \sigma_0 e^{-\frac{E_a}{K_B T}}. \tag{12}$$

The activation energy obtained from the linear fitting is E_a = 0.53 eV. This value closely matches that derived from the

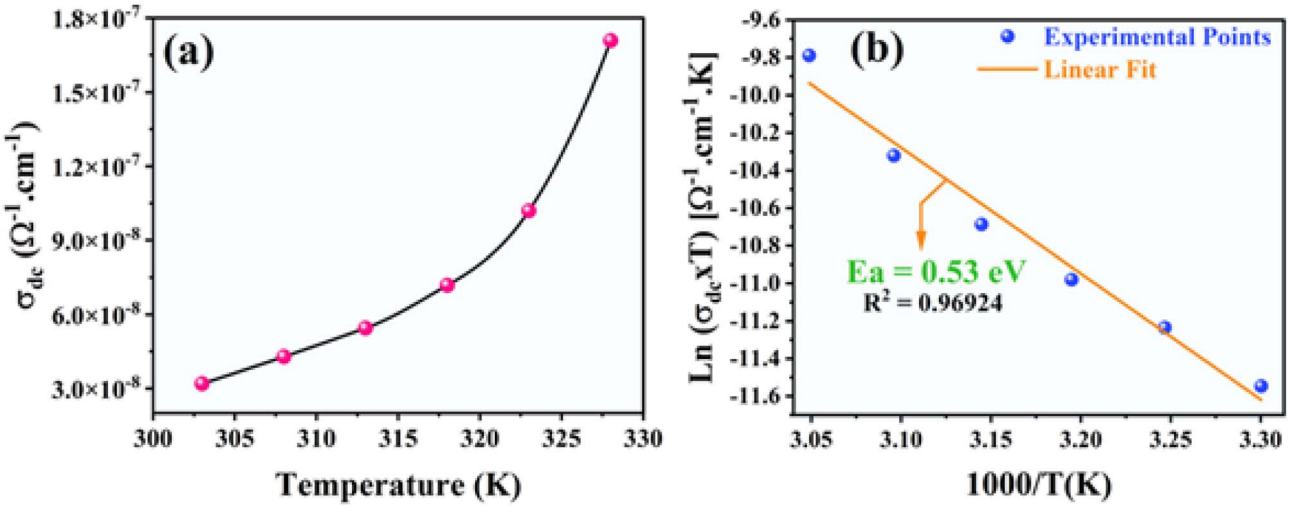

Fig. 12 (a) Temperature dependence of DC conductivity for the $(P(C_4H_9)_4)_2[ZnBr_4]$ compound. (b) Plot of ln ($\sigma_{dc} \times T$) *versus* 1000/*T*.

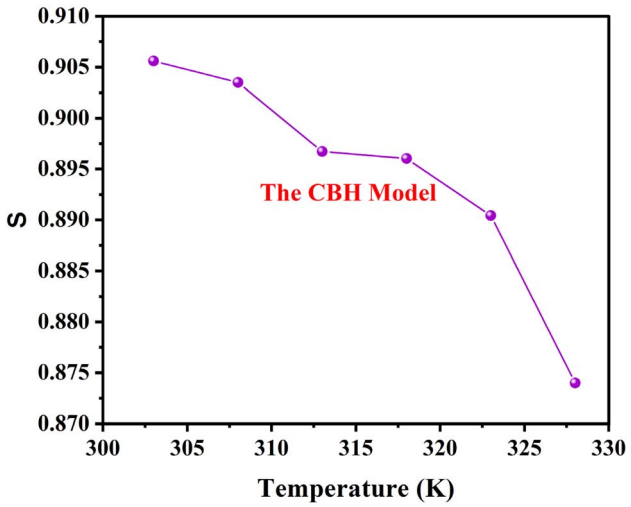

Fig. 13 Variation of the universal exponent "s" as a function of the temperature.

resistance parameter, suggesting that low-frequency conductivity is primarily governed by grain boundary effects.

To gain insight into the conduction mechanism within $(P(C_4H_9)_4)_2[ZnBr_4]$, several theoretical models have been put forward to explain the temperature-dependent behavior of the exponent "s". These include the correlated barrier hopping (CBH), quantum mechanical tunneling (QMT), non-overlapping small polaron tunneling (NSPT), and overlapping large polaron tunneling (OLPT) models. Fig. 13 shows the temperature dependence of the exponent s; as temperature rises, s decreases until it reaches a minimum value. This behavior aligns with the predictions of the correlated barrier hopping (CBH) model. Additionally, when $s < 1$, it suggests that the conduction mechanism is primarily governed by hopping, which arises from the translational motion of charge carriers.[51]

3.5.3 Electrical capacitance and relaxation dynamics. Capacitance measurements were performed over identical angular frequency and temperature intervals. Fig. 14(a) presents the temperature-dependent variation of capacitance $C(\omega)$ for the $(P(C_4H_9)_4)_2[ZnBr_4]$ compound. In the low-frequency domain ($\omega < 10^4$ rad s^{-1}), a significant temperature sensitivity is observed, which is often accompanied by pronounced dispersion. This behavior is commonly attributed to charge and ion accumulation at the electrode interfaces, likely resulting from electrode polarization effects. Moreover, the nearly linear capacitance response within the frequency range of $\omega < 10^4$ rad s^{-1} suggests a decrease in space charge density. Previous findings[52] indicate that an increase in capacitance with increasing temperature is related to reduced bond strength. Higher thermal energy enhances orientational vibrational activity and weakens interatomic forces, thereby increasing the material's polarizability and, consequently, its capacitance. At higher frequencies ($\omega > 10^4$ rad s^{-1}), the capacitance curve reaches a plateau, indicating the diminished contribution of space charge and polarization mechanisms. It is also important to note that the separation between electrodes plays a crucial role in influencing the dielectric behavior of the material.[53]

Complex electric modulus formalism offers an alternative method for analyzing a material's electrical behavior. This approach allows for the separation of various contributions, such as electrode polarization, charge transport, and relaxation processes, occurring within grains and across grain boundaries. The complex electric modulus $M^*(\omega)$ is defined as the inverse of the complex permittivity, expressed as follows:[41]

$$M^*(\omega) = M'(\omega) + jM''(\omega). \quad (13)$$

Fig. 14(b) illustrates the frequency-dependent variations of the imaginary component of the electric modulus for the $(P(C_4H_9)_4)_2[ZnBr_4]$ sample in the temperature range of 303–328 K. An examination of the plot reveals a distinct relaxation peak. As the temperature increases, the position of the peak

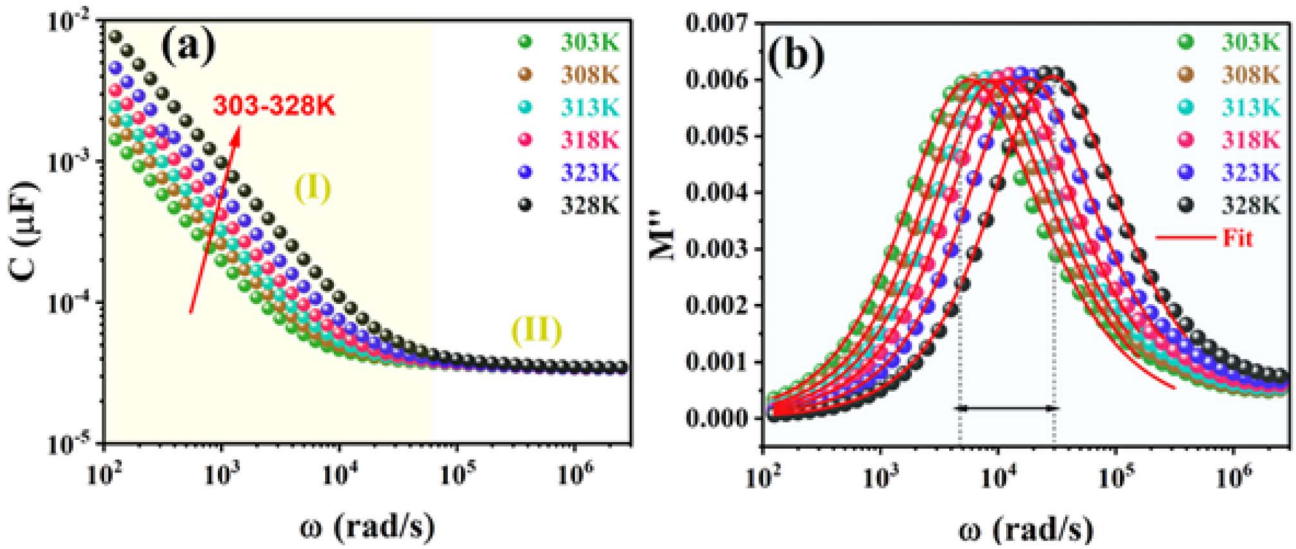

Fig. 14 Frequency dependence of the capacitance (a) and modulus (b) at various temperatures for the $(P(C_4H_9)_4)_2[ZnBr_4]$ compound.

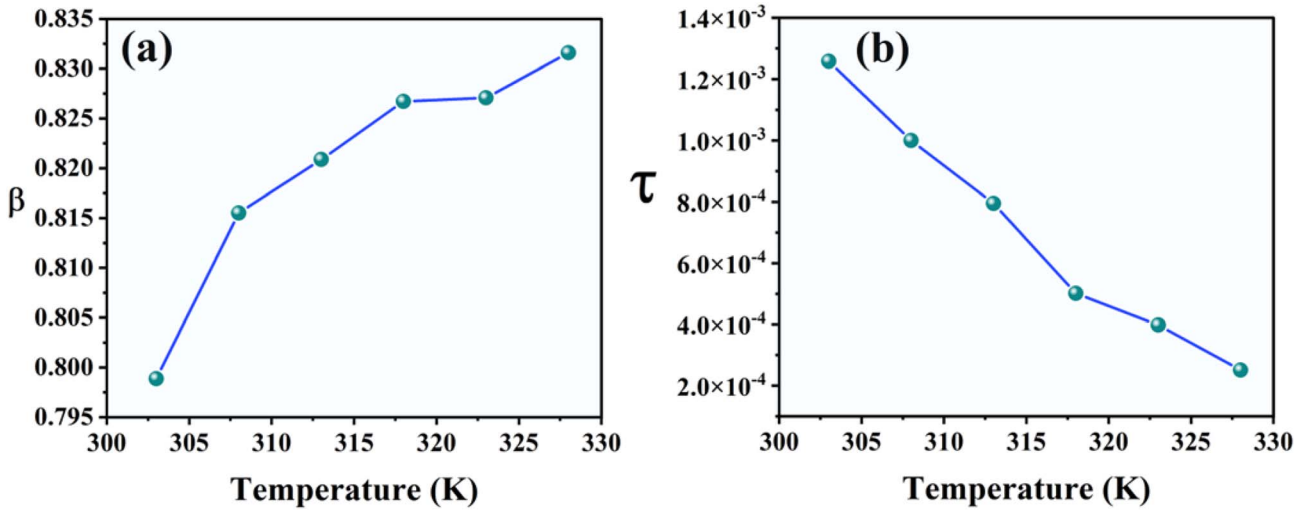

Fig. 15 (a) Variation of the exponent β as a function of the temperature. (b) Variation of "τ" as a function of the temperature.

maximum M'' max shifts toward higher frequencies, accompanied by peak broadening, which is an indication of the material's ionic conducting nature.[54] The asymmetric shape of the peak suggests a distribution of relaxation times, which is characteristic of a non-Debye relaxation mechanism.[55] To further analyze the relaxation behavior across different temperatures, the imaginary component M'' of the electric modulus was fitted using an approximate frequency-dependent expression of the Kohlrausch–Williams–Watts (KWW) function, as formulated by Bergman as follows:[56]

$$M''(\omega) = \frac{M''_{\max}(\omega)}{\left[1-\beta+\left(\frac{\beta}{\beta+1}\right)\left[\beta\left(\frac{\omega_{\max}}{\omega}\right)+\left(\frac{\omega}{\omega_{\max}}\right)^{\beta}\right]\right]}. \quad (14)$$

For compound $(P(C_4H_9)_4)_2[ZnBr_4]$, the β parameter remains below 1 throughout the examined temperature range. An upward trend in β with increasing temperature suggests a non-Debye-type conduction mechanism, as depicted in Fig. 15(a). Meanwhile, Fig. 15(b) presents the variation in the relaxation time (τ) as a function of temperature. The presence of space charge effects in $(P(C_4H_9)_4)_2[ZnBr_4]$ is inferred from the microsecond scale of τ, as space charges typically exhibit relaxation times within this range. According to the literature, such space charges arise due to the redistribution of charge carriers within the crystal lattice. The observed decline in τ with increasing temperature suggests enhanced thermal delocalization of these carriers in $(P(C_4H_9)_4)_2[ZnBr_4]$.[57] This thermal activation implies a transition from non-Debye to Debye-like relaxation behavior at elevated temperatures.[58]

Fig. 16 displays the plot of $\ln(\tau \times T)$ *versus* $(1000/T)$, revealing a trend that follows the Arrhenius law. Based on this analysis, the calculated activation energy is 0.52 eV, which closely matches the value derived from DC conductivity studies. This strong correlation indicates that both the relaxation dynamics and the conduction process share a common underlying mechanism.[47]

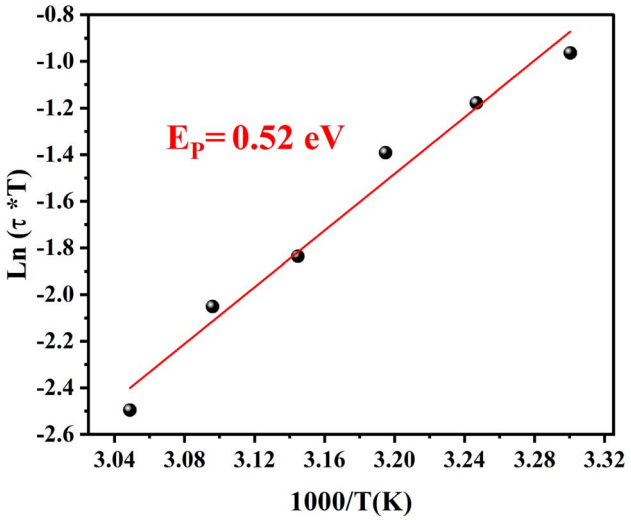

Fig. 16 Variation of $\ln(\tau \times T)$ *versus* $1000/T$.

3.6. Dielectric study

The dielectric characteristics of a material represent a fundamental aspect of its physical description because they significantly affect its response in electrical and electromagnetic environments. These properties are closely associated with the polarizability of the molecules that compose the material. Such polarizability results from the combined action of several polarization mechanisms, including ionic, electronic, orientational, and space-charge contributions, each playing a specific role in determining the overall dielectric response of the system.[59] The dielectric constant of a material can therefore be expressed in its complex form as follows:[60]

$$\varepsilon = \varepsilon_r + i\varepsilon_i, \quad (15)$$

where ε_r denotes the material's capacity to store energy *via* dipole orientation and ionic/electronic polarization and ε_i

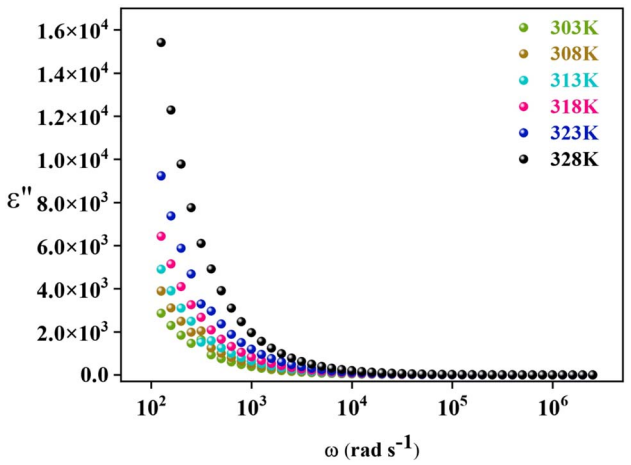

Fig. 17 Dielectric loss (ε'') as a function of the frequency.

denotes energy losses due to resistive effects from charge movement or dipole realignment.[61,62]

The variation of the imaginary part of the dielectric permittivity (ε'') as a function of angular frequency over a temperature range of 303–328 K is shown in Fig. 17

The behavior of the dielectric constant (ε_r) is essential when designing several electronic devices. These parameters define the energy storing capacity when the material interacts with an external electric field.[63] As illustrated in this figure (Fig. 17), ε'' increases with temperature and progressively decreases as the frequency increases. In the low-frequency region, the dielectric constant shows high values and a clear dispersive behavior. This phenomenon is mainly attributed to space-charge polarization caused by the accumulation of charge carriers at the electrode–sample interface. At low frequencies, the charge carriers have enough time to move and accumulate, which increases polarization. However, as the frequency increases, the electric field changes more rapidly, and the dipoles are no longer able to follow these variations.[64,65] Consequently, the contribution of this polarization decreases, leading to a reduction in both the dielectric constant and the dielectric loss. Materials with high dielectric constants are of great interest for electronic applications because they can store more electrical energy and improve the performance of electronic devices.[66]

4 Conclusion

Slow evaporation at room temperature was used to successfully create a new organic–inorganic hybrid, $(P(C_4H_9)_4)_2[ZnBr_4]$. Various characterization techniques were employed to investigate the structural, vibrational, and electrical properties of the compound. Single-crystal X-ray diffraction analysis reveals that the compound crystallizes in the monoclinic system with the $P2_1/c$ space group. Its structure comprises two crystallographically independent organic $(P(C_4H_9)_4)^+$ cations and one type of isolated $[ZnBr_4]^{2-}$ anion. Each tetrahedral $[ZnBr_4]^{2-}$ anion is surrounded by three tetrabutylphosphonium cations, forming multiple C–H···Br contacts that reinforce the structural framework. The molecular structure and vibrational properties calculated at the DFT/B3LYP/LanL2DZ/6-311G(d,p) level of theory are in excellent agreement with the experimental data. This strong correspondence confirms the reliability of the computational approach and allows an unambiguous assignment of all observed IR and Raman vibrational modes in the present work. Electrical investigations demonstrate that the conductivity of $(P(C_4H_9)_4)_2[ZnBr_4]$ is thermally activated and follows Arrhenius behavior, with an activation energy (E_a) of 0.53 eV. This temperature-dependent conduction mechanism clearly confirms the semiconducting character of the material. Moreover, the charge transport behavior was consistent with the correlated barrier hopping (CBH) model, as evidenced by the temperature-dependent variation of the frequency exponent *s*. The asymmetric shape of the imaginary electric modulus spectrum, well described by the Kohlrausch–Williams–Watts model, further validates the non-Debye relaxation process. The dielectric properties are useful for energy storage applications. All the above electrical and dielectric properties of the $(P(C_4H_9)_4)_2[ZnBr_4]$ have potential use in the field of optoelectronic and dielectric applications.

Author contributions

Molka Ezzedine: writing – original draft, validation, software, methodology, and investigation. Malika Ben Gzaiel: writing – original draft, validation, software, methodology, and investigation. Mohamed Tliha: writing – original draft, visualization, and formal analysis. E. López-Lago. formal analysis, validation, and writing – review. Walid Rekik: writing – review and editing, visualization, and validation. Ali Ben Ahmed: writing – review and editing, visualization, and validation. Abderrazek Oueslati: writing – review and editing, visualization, validation, investigation, formal analysis, and data curation.

Conflicts of interest

The authors declare that they have no known competing financial interests or personal relationships that could have appeared to influence the work reported in this paper.

Data availability

CCDC 2426791 contains the supplementary crystallographic data for this paper.[67]

Data will be made available upon request.

Supplementary information (SI) is available. See DOI: https://doi.org/10.1039/d6ra00849f.

Funding

This research work was funded by Umm Al-Qura University, Saudi Arabia under grant number: 26UQU4331138GSSR05.

Acknowledgements

The authors extend their appreciation to Umm Al-Qura University, Saudi Arabia for funding this research work through grant number: 26UQU4331138GSSR05.

References

1 I. Garoui, S. Hajlaoui, M. Tliha, R. Naouari, S. Nasri, A. Ouasri, J. Lhoste and A. Oueslati, New organic–inorganic chloride (2-amino-4-methylpyridinium hexachlorostannate): Crystal structure, BFDH morphology, and electrical conduction mechanism, *J. Phys. Chem. Solids*, 2025, **206**, 112840.

2 M. Khawla, A. Dhouha, D. Ikram, E. Slim, O. Ali and E. Zakaria, A 0D lead-free Nickel halide-based perovskite exhibiting greenish light emission and high color rendering index, *Mater. Res. Bull.*, 2023, **167**, 112396.

3 M. Catauro and S. Vecchio Ciprioti, Sol-Gel Synthesis and Characterization of Hybrid Materials for Biomedical Applications, *J. Mol. Struct.*, 2019, 445–475.

4 L. T. López, D. Ramírez, F. Jaramillo and J. A. Calderón, Novel hybrid organic-inorganic CH3NH3NiCl3 active material for high-capacity and sustainable lithium-ion batteries, *Electrochim. Acta*, 2020, **357**, 136882.

5 M. Alktranee and P. Bencs, Overview of the hybrid solar system, *Anal. Tech. Szeged.*, 2020, **14**, 100–108.

6 I. Ibrahmi, A. Oueslati, F. N. Almutairi and M. Mallek, Synthesis and trigonal structure of a new lead-free zero-dimensional perovskite (CH3NH3)2[SnBr6] with multifunctional optical and electrical properties, *J. Phys. Chem. Solids*, 2025, **207**, 112909.

7 K. Karim, F. Hajlaoui, N. Audebrand, T. Roisnel and A. Ben Rhaiem, Synthesis, Crystal Structures, High-Temperatures Phase Transition, Optic and Electric Properties of Hybrid Halogenometallates: [(CH3)3N(CH2)2Br]2[MIIBr4] (M = Cu, Zn), *J. Alloys Compd.*, 2020, **844**, 156115.

8 M. Ben Bechir, K. Karoui, M. Tabellout, K. Guidara and A. Ben Rhaiem, Alternative Current Conduction Mechanisms of Organic-Inorganic Compound [N(CH3)3H] 2CuCl4, *J. Appl. Phys.*, 2014, **115**(20), 203712.

9 M. Khalfa, A. Oueslati, K. Khirouni, M. Gargouri, S. Auguste, J. F. Bardeau and G. Corbel, New Organic–Inorganic Bromides [(C3H7)4N]2MBr4 (M=Hg and Cd): Synthesis, Crystal Structure and Vibrational Characterization, *J. Alloys Compd.*, 2025, **1034**, 181334.

10 C. Souad and A. Aydi, Electrical Conductivity and Vibrational Studies Induced Phase Transition in [N(C3H7)4]2ZnBr4 Compound, *J. Adv. Dielectr.*, 2021, **11**(1), 2150005.

11 C. Na and Ae R. Lim, Elucidation of Crystal Growth, Structural Characterization, Thermal Properties, and Molecular Dynamics Using NMR near Phase Transition Temperature of [N(CH3)4]2CoCl4, *Sci. Rep.*, 2025, **15**(1), 11360.

12 F. Yuan, X. Liu, S. Zhang, P. Zhu, F. Ali, C. Zhao and S. He, Efficient and Stable Deep-Blue 0D Copper-Based Halide TEA2Cu2I4 with Near-Unity Photoluminescence Quantum Yield for Light-Emitting Diodes, *Nanomaterials*, 2024, **14**(23), 1919.

13 H. Elgahami, A. Oueslati, S. Nasr, F. Costantino and H. Naïli, On the High-Temperature Phase Transition of a New Chlorocadmate(ii) Complex Incorporating Symmetrical Cd2Cl6 Clusters: Structural, Optical and Electrical Properties, *RSC Adv.*, 2023, **13**(37), 26122–26133.

14 X. Meng, H. Li, Y. Zhao and W. Zhang, Metal regulated organic–inorganic hybrid ferroelastic materials: [(CH3)CN(CH3)2CH2F]2[MBr4] (M = Cd and Zn), *Inorg. Chem. Front.*, 2022, **9**, 1603–1608.

15 H. Sakiyama, T. Abiko, M. Ito, R. Mitsuhashi, M. Mikuriya and K. Waki, Conformational analysis of an octahedral zinc(II) complex with six dimethylsulfoxide, *Polyhedron*, 2016, **119**, 512–516.

16 C. Sanchez, B. Julián, P. Belleville and M. Popall, Applications of hybrid organic–inorganic nanocomposites, *J. Mater. Chem.*, 2005, **15**, 3559.

17 M. Mallek, I. Garoui, F. N. Almutairi, I. Chaabane, W. Rekik and A. Oueslati, Synthesis, structural characterization, Hirshfeld surface analysis, and electrical properties of a zinc (II)- based organic–inorganic hybrid compound, *J. Mater. Sci.: Mater. Electron.*, 2025, **36**, 485.

18 M. E. G. Hemade, I. Garoui and F. N. Almutairi, Synthesis, structural analysis, spectroscopic characterization and optical properties of bis(4-acetylanilinium) tetrabromorozincate (II), *J. Mol. Struct.*, 2025, **1345**, 143098.

19 A. R. Lim, Physicochemical properties of the cation in organic–inorganic perovskite [NH3(CH2)4(NH3)]ZnBr4 crystals investigated using 1H and 13C nuclear magnetic resonance relaxation, *J. Solid State Chem.*, 2021, **302**, 122438.

20 H. Khachroum, M. Krimi, M. S. M. Abdelbaky, S. García-Granda and M. Dammak, A comprehensive study of crystal structure, UV–visible study, electric-dielectric properties of a recently developed Hybrid Material [(C6H5N2)2ZnCl4], *Mater. Res. Bull.*, 2024, **179**, 112978.

21 I. Garoui, A. Oueslati, M. Mallek and F. N. Almutairi, Synthesis, crystal structure, BFDH morphology, Hirshfeld surface analysis and electrical characterization of the new bi-(2-amino-5-methylpyridinium) hexa-chlorostannate compound, *Phys. E*, 2024, **158**, 115897.

22 G. M. Sheldrick, *SADABS*, Bruker AXS Inc., Madison, Wisconsin, USA, 2014.

23 G. M. Sheldrick, SHELXT–Integrated space-group and crystal-structure determination, *Acta Crystallogr. A*, 2015, **71**, 3–8.

24 G. M. Sheldrick, Crystal structure refinement with SHELXL, *Acta Crystallogr. C*, 2015, **71**, 3–8.

25 L. J. Farrugia, WinGX suite for small-molecule single-crystal crystallography, *J. Appl. Crystallogr.*, 1999, **32**, 837–838.

26 K. Brandenburg, *Diamond, Version 3.2i*, Crystal Impact GbR, Bonn, Germany, 2004.

27 L. Yang, D. R. Powell and R. P. Houser, Structural variation in copper(I) complexes with pyridylmethylamide ligands: structural analysis with a new four-coordinate geometry index, τ_4, *Dalton Trans.*, 2007, **9**, 955–964.

28 W. H. Baur, The geometry of polyhedral distortions. Predictive relationships for the phosphate group, *Acta Crystallogr. B*, 1974, **30**, 1195–1215.
29 M. Ines, M. B. Gzaiel, A. Oueslati, S. Auguste, J. Lhoste and M. Gargouri, Crystal structure and electrical conduction mechanism of the new bi-tetrabutylphosphonium hexachlorostannate compound, *J. Mol. Struct.*, 2021, **1226**, 129361.
30 F. M. Laoui, F. Balegroune, F. Saib, C. Charles and M. Trari, Synthesis, characterizations, photo-electrochemical, and physical properties of a new 0D copper(II) complex, *J. Mater. Sci.: Mater. Electron.*, 2022, **33**(15), 11701–11711.
31 J. Faber, EPDIC-8, European Powder Diffraction Conference, *Powder Diffr.*, 2002, **17**(4), 337–338.
32 A. D. Becke, Density-functional thermochemistry. III. The role of exact exchange, *J. Chem. Phys.*, 1993, **98**, 5648–5652.
33 C. Lee, W. Yang and R. G. Parr, Development of the Colle–Salvetti correlation-energy formula into a functional of the electron density, *Phys. Rev. B*, 1988, **37**, 785–789.
34 M. J. Frisch *et al.*, *Gaussian 16, Revision C.01*, Gaussian, Inc., Wallingford CT, 2016.
35 P. J. Hay and W. R. Wadt, Ab initio effective core potentials for molecular calculations. Potentials for the transition metal atoms Sc to Hg, *J. Chem. Phys.*, 1985, **82**, 270–283.
36 A. P. Scott and L. Radom, Harmonic vibrational frequencies: An evaluation of Hartree–Fock, Møller–Plesset, quadratic configuration interaction, density functional theory, and semiempirical scale factors, *J. Phys. Chem.*, 1996, **100**, 16502–16513.
37 S. Chkoundali, I. Garoui, W. Trigui and A. Oueslati, Crystal structure, Hirshfeld surface analysis, conduction mechanism and electrical modulus study of the new organic–inorganic compound [C8H10NO]2HgBr4, *RSC Adv.*, 2024, **14**, 8971–8980.
38 I. Garoui, M. Mallek, F. N. Almutairi, W. Rekik and A. Oueslati, Synthesis, Structural characterization and complex impedance analysis of a novel organic-inorganic hybrid compound based on Mercury (II) chloride, *J. Mol. Struct.*, 2024, **1315**, 138881.
39 D. Johnson, *ZPlot, ZView Electrochemical Impedance Software, Version 2.3 B*, Scribner Associates Inc., North Carolina, 2000.
40 M. Javed, Y. Moualhi, N. Akbar, A. Masood, T. Alomayri and S. A. Muhammed Ali, Electrical dynamics and Havriliak-Negami dielectric relaxation behavior of FeNi2O4 electromagnetic spinel nickelate, *Ceram. Int.*, 2025, **25**, 1256.
41 M. Javed, Y. Moualhi, N. Akbar, T. Alomayri and S. A. Muhammed Ali, Temperature dependent impedance spectroscopy and electrical transport mechanism in sol-gel derived MgCr2O4 spinel oxide, *Phys. B*, 2020, **599**, 412377.
42 M. B. Bechir, A. Almeshal and M. H. Dhaou, Structural evolution, dielectric relaxation, and charge transport characteristics of formamidinium lead iodide (FAPbI3) perovskite, *Mater. Res. Bull.*, 2023, **157**, 112012.
43 H. Rahmouni, M. Smari, B. Cherif, E. Dhahri and K. Khirouni, Conduction mechanism, impedance spectroscopic investigation and dielectric behavior of manganites with compositions below the concentration limit of silver solubility in perovskites ($0 \leq x \leq 0.2$), *Dalton Trans.*, 2015, **44**, 10457–10466.
44 S. Ben Yahya, I. Garoui, M. Zaghrioui, A. Oueslati and B. Louati, Solid-state synthesized Li4GeO4 germanate: an exploration of its structure, vibrational characteristics, electrical conductivity, and dielectric properties, *RSC Adv.*, 2025, **15**, 9295–9304.
45 H. Khachroum, M. Krimi, M. S. M. Abdelbaky, S. García-Granda and M. Dammak, A comprehensive study of crystal structure, UV-visible study, electric-dielectric properties of a recently developed Hybrid Material [(C6H5N2)2ZnCl4], *Mater. Res. Bull.*, 2024, **179**, 112978.
46 M. Ben Gzaiel, I. Garoui, F. N. Almutairi, I. Mbarek and O. A, Lead-Free halide perovskites for optoelectronic application: Investigation of structural, optical, electric and dielectric behaviors, *Opt. Mater.*, 2024, **154**, 115664.
47 M. M. Bouzayani, I. Soudani, M. B. Abdessalem, S. Znaidia, A. Oueslati and A. Aydi, Electrical conduction mechanism and dielectric properties of the KSr0.5Fe2O4 spinel ferrite, *J. Mater. Sci.: Mater. Electron.*, 2024, **35**, 1256.
48 D. K. Pradhan, P. Misra, V. S. Puli, S. Sahoo, D. K. Pradhan and R. S. Katiyar, Studies on structural, dielectric, and transport properties of Ni0.65Zn0.35Fe2O4, *J. Appl. Phys.*, 2014, **115**, 243904.
49 A. K. Jonscher, The 'universal' dielectric response, *Nature*, 1977, **267**, 673–679.
50 I. Gharbi, A. Ghoudi, I. Kammoun, A. Mahmoud and A. Oueslati, Dielectric relaxation and charge transfer mechanism of the inorganic perovskite CsHgCl3, *Inorg. Chem. Commun.*, 2024, **166**, 112565.
51 J. H. Joshi, D. K. Kanchan, M. J. Joshi, H. O. Jethva and K. D. Parikh, Dielectric relaxation, complex impedance and modulus spectroscopic studies of mix phase rod like cobalt sulfide nanoparticles, *Mater. Res. Bull.*, 2017, **93**, 63–73.
52 A. Kalam, M. Javed, Y. Moualhi, N. Akbar and A. Masood, Interpretation of Resistance, Capacitance, Defect Density, and Activation Energy Levels in Single-Crystalline MAPbI3, *J. Phys. Chem. C*, 2020, **124**, 3496–3502.
53 S. Eom, P. Kavle, D. Kang, Y. Kim, L. W. Martin and S. Hong, Unveiling the Nanoscale Dielectric Gap and Its Influence on Ferroelectric Polarization Switching in Scanning Probe Microscopy, *Adv. Funct. Mater.*, 2024, **35**, 202406944.
54 M. Javed, Y. Moualhi, N. Akbar, T. Alomayri and S. A. Muhammed Ali, Dielectric relaxation and small polaron hopping transport in sol-gel-derived NiCr2O4 spinel chromite, *Mater. Res. Bull.*, 2021, **138**, 111242.
55 B. Kaur, L. Singh, V. A. Reddy, D.-Y. Jeong, N. Dabra and J. S. Hundal, AC Impedance Spectroscopy, Conductivity and Optical Studies of Sr doped Bismuth Ferrite Nanocomposites, *J. Asian Ceram. Soc.*, 2016, **11**, 4120–4135.
56 R. Bergman, General susceptibility functions for relaxations in disordered systems, *J. Appl. Phys.*, 2000, **88**, 1356–1365.
57 M. Ben Bechir and F. Alresheedi, Interpretation of dielectric behavior and polaron hopping in lead-free antimony-based double perovskite, *RSC Adv.*, 2023, **13**, 34703–34714.

58 M. Ben Bechir and M. H. Dhaou, Study of charge transfer mechanism and dielectric relaxation of all-inorganic perovskite CsSnCl3, *RSC Adv.*, 2021, **11**, 21767–21780.
59 P. C. Kumar, S. Subrata, P. Debidutta, J. Kumar and R. Naik, A Facile One-Step Microwave-Assisted Synthesis of Bismuth Oxytelluride Nanosheets for Optoelectronic and Dielectric Application: An Experimental & Computational Approach, *J. Alloys Compd.*, 2023, **968**, 172166.
60 S. Supriya, S. Das, S. K. Samal, S. Senapati and R. Naik, Rapid Microwave-Assisted Synthesis and Characterization of a Novel CuCoTe Nanocomposite Material for Optoelectronic and Dielectric Applications, *Nanoscale*, 2024, **16**(15), 7566–7581.
61 S. Das, S. Senapati, S. K. Samal and R. Naik, Novel Cu1+xMn1-XSeTe Nanostructure Fabrication by Simple Microwave Synthesis for Potential Photodetection and Dielectric Applications, *Surf. Interfaces*, 2025, **56**, 105507.
62 V. D. Nithya and R. Kalai Selvan, Synthesis, Electrical and Dielectric Properties of FeVO4 Nanoparticles, *Phys. B*, 2011, **406**(1), 24–29.
63 C. R. Cena and A. Kumar Behera, Banarji Behera, Structural, Dielectric, and Electrical Properties of Lithium Niobate Microfibers, *J. Adv. Ceram.*, 2016, **5**(1), 84–92.
64 D. Sahoo, S. Senapati, S. Samal, S. Varadharajaperumal and R. Naik, Optical and Dielectric Characterization of Nanoparticle-Based Cu2Ni1+xSn1−xS4 Nanosphere Synthesized by Facile Solvothermal Method, *ACS Appl. Eng. Mater.*, 2023, **1**, 1001–1012.
65 A. Parida, S. Senapati, G. K. Pradhan and R. Naik, Tailoring Optical Properties of Hydrothermally Synthesized SnMnSe Nanocubes for Optoelectronic and Dielectric Applications, *J. Alloys Compd.*, 2024, **970**, 172520.
66 A. Behera, S. A. Khan, F. Singh, P. C. Kumar, R. Naik, R. Biswal and P. Mallick, Effect of 90 MeV Oxygen and Carbon Ion Irradiation on Structural, Optical and Dielectric Properties of ZnO Embedded in PVA Matrix, *Phys. Scr.*, 2025, **100**(3), 035951.
67 CCDC 2426791: Experimental Crystal Structure Determination, 2026, DOI: 10.5517/ccdc.csd.cc2mg8lz.